Lattice-guided assembly of optoelectronically-active π-conjugated peptides on 1D van der Waals single crystals

Ze-Fan Yao,[1,2] Dmitri Leo Mesoza Cordova,[2] Griffin M. Milligan,[2] Diana Lopez,[2] Steven Jay Allison,[2] Yuyao Kuang,[1] Herdeline Ann M. Ardoña,[1,2,3,4]* Maxx Q. Arguilla[1,2]*

Affiliation:

[1]Department of Chemical and Biomolecular Engineering, Samueli School of Engineering, University of California, Irvine, CA 92697, USA

[2]Department of Chemistry, School of Physical Sciences, University of California, Irvine, CA 92697, USA

[3]Department of Biomedical Engineering, Samueli School of Engineering, University of California, Irvine, CA 92697, USA

[4]Sue & Bill Gross Stem Cell Research Center, University of California, Irvine, CA 92697, USA

*Corresponding authors:

E-mail: Herdeline Ann M. Ardoña hardona@uci.edu; Maxx Q. Arguilla marguill@uci.edu

Keywords: One-dimensional materials, van der Waals solids, peptides, conjugated molecules, photocurrent, self-assembly

Abstract: The utility of organic functional units for high-performance materials and devices is highly dependent on the formation of ordered domains across extended regimes. As such, the development of synthetic approaches to achieve precisely ordered material building blocks, a process often complicated by the dynamic and sensitive nature of supramolecular interactions in many organic molecules, is critical in realizing efficient functional devices and emergent physical properties. To this end, we leveraged the long-range anisotropic ordering intrinsic to a class of 1D van der Waals (vdW) crystals comprised of sub-nanometer-thick transition metal trichalcogenide (MCh_3; M = Ti, Zr, Hf, Nb, Ta; Ch = S, Se) chain subunits to guide the assembly of supramolecular π-conjugated peptide building blocks. Through this synthetic strategy, we realized morphologically well-defined organic-inorganic heterointerfaces that display drastically altered photophysical properties and are capable of photocurrent generation. Owing to the structural correspondence between the π-π interactions of the organic quaterthiophene (4T)-based π-conjugated peptides (DDD-4T) and the periodic sulfur ordering along the (100) planes of inorganic niobium sulfide (NbS_3) 1D vdW crystals, we found that organic π-conjugated peptide monomers can readily form 1D supramolecular assemblies on the surface of the underlying inorganic crystal. Optimal assembly conditions allowed for the controlled deposition and growth of the peptide assemblies on the crystal surfaces as validated by a combination of fluorescence microscopy, photoluminescence mapping, Raman spectroscopy, atomic force microscopy, and computational molecular dynamics simulations. The resulting DDD-4T/NbS_3 heterointerfaced assemblies exhibit a significantly improved visible-range photocurrent generation compared to the freestanding π-conjugated peptide films assembled from solution. Altogether, our study demonstrates the important role of lattice matching in the formation of ordered low-dimensional organic-inorganic heterointerfaces, offering a new approach towards directing the assembly of supramolecular organic building blocks endowed with improved optical and optoelectronic properties.

Introduction

The molecular ordering of functional molecules, such as π-conjugated molecules and peptides, across various spatial scales plays a vital role in determining their charge and energy transport capabilities in various applications, including light harvesting, sensing, and biointerfacing (*1–6*). Since efficient charge and energy transport requires the facilitation of delocalized electrons across neighboring molecules, precise control over self-assembly and long-range ordering of organic molecules is paramount towards achieving efficient electronic functionalities (*7–9*). However, navigating the complex landscape of assemblies formed by organic molecules from dissolved monomers in solutions to ordered aggregates in solid device interfaces remain a challenge, primarily stemming from the dynamic and highly sensitive nature of supramolecular interactions. To this end, it has been recognized that controlling the self-assembly of optoelectronic units is critical to the formation of long-range ordering, where the non-covalent interactions including, hydrogen bonding, van der Waals (vdW) forces, and π-π interactions, need to be modulated *via* molecular design or external factors (*1–3*, *10*). Therefore, gaining the synthetic ability to influence the noncovalent molecular interactions that govern the long-range assembly of organic monomers in solution would advance diverse fields ranging from supramolecular chemistry to optoelectronics that approach the sub-nanometer regime (*11–14*).

A reliable approach for influencing molecular ordering at the meso- to microscale is to involve architectured surfaces comprised of patterned inorganic substrates, block polymers, nanoparticles, or other organic and biomolecular self-assembly templates (*15–17*). Among the hybrid materials that arise from templating, the creation of organic-inorganic heterointerfaces has enabled the assembly of organic structures that bear considerably altered optoelectronic properties due to interfacial exciton transfer and carrier transport with the underlying inorganic substrate (*14*, *18–23*). In recent examples, 2D inorganic vdW surfaces that bear atomically precise and flat surfaces have been shown to template the assembly of heterointerfaced organic molecules with endowed non-native ordering motifs, such as high-symmetry planar hexagonal packing (*22*, *23*). For instance, Huang, Yoreo, and coworkers demonstrated that inorganic MoS_2 (0001) surface could assist the hexagonal assembly growth of peptides with a reduced nucleation barrier (*24*). Claridge and coworkers, on the other hand, systemically studied the formation of lamellar nanostructures with distinct patterns of polydiacetylenes on 2D highly ordered pyrolytic graphite (HOPG) (*25*, *26*). Furthermore, Wang and coworkers achieved 2D polymer/MoS_2 heterostructures with controlled photoluminescence and electronically coupled semiconducting properties, which provided key insights into electroactive vdW heterostructures based on organic polymers and 2D transition-metal dichalcogenides (*27*). These examples collectively demonstrate that organic molecules can readily form controlled assemblies with suitable inorganic templates, providing unique organic-inorganic heterointerfaces with strongly modulated physical properties.

Whereas 2D vdW surfaces provide atomically flat surfaces ideal for molecular assembly, the intrinsic two-dimensional geometric and crystalline limitation imposed by their underlying crystal structures hinders the continuous assembly of polymeric or peptidic structures that naturally possess 1D order. In recent years, we have seen the rediscovery of an underexplored class of 1D and quasi-1D vdW solids. These materials illustrate that similar vdW interactions which lead to atomic precision and exfoliability in 2D vdW solids could also exist between stable 1D sub-units (*28–31*). The rediscovery of several families of 1D or quasi-1D vdW solids, typically characterized by weakly bound continuous chains with sub-nanometer cross-sections, has led to the realization of nascent physical phenomena including unconventional superconductivity (*32*), defect-tolerant dissipationless photocurrent (*33*), topologically protected states (*34*, *35*), high-fidelity electrical transport (*36*), as well as a recent demonstration of emergent optical states upon 1D confinement (*37*). Among these, 1D vdW transition metal trichalcogenides (MCh_3; M = Ti, Zr, Hf, Nb, Ta; Ch = S, Se) have served as model phases to explore the chemistry and physics in low dimensions due to their highly modular structures (*31*), rich polymorphism (*38*), and the presence of diverse electronic and optical states (*39–41*). Beyond their 1D crystalline nature, MCh_3 1D vdW crystals such as NbS_3 have been demonstrated to be chemically, thermally, and mechanically stable, making them ideal platforms for interfacing with solution-based organic monomers (*42–44*). Together, the dimensional complementarity between the highly crystalline 1D vdW solids and the intrinsic 1D ordering of supramolecular organic materials through long-range cooperative noncovalent interactions provides a suitable means to direct the self-assembly of functional organic molecules into 1D organic- 1D inorganic heterointerfaces with long-range order.

In this report, we demonstrate that the surface assembly of organic π-conjugated peptides can be controlled by the atomically defined lattice topography of a model inorganic 1D vdW MCh_3 single crystal, NbS_3. Symmetric peptide-π-peptide units can afford the assembly into 1D chiral nanostructures in solution due to non-covalent interactions such as π-π interactions and hydrogen bonding. To guide the assembly of these π-conjugated peptides into ordered structures that are effectively photoconductive, we take advantage of the geometric similarity between the assembly process of π-conjugated peptides (with π-π interactions around 3.5 Å) and the periodic lattice spacing (3.4 Å) of the (001) lattice planes in NbS_3 (Figure 1A). We establish herein the 1D assembly of highly ordered π-conjugated peptide on the NbS_3 crystal surface through this lattice-guided strategy. We further show that the growth and deposition of the peptide assemblies on the crystal surface are controlled by tuning the assembly conditions, especially the incubation and deposition time of the NbS_3 crystal with the monomer solution. A suite of structural, spectroscopic, and device characterization, as well as computational simulation, support the feasibility of controlled 1D growth of organic π-conjugated peptides on the inorganic crystals. Moreover, the resulting organic-inorganic heterostructures of π-conjugated peptides and vdW crystals demonstrate improved photocurrent generation under illumination upon interfacing, showing a significant enhancement in photocurrent compared to the dropcasted film of the bare π-conjugated peptides. Overall, this work accomplishes the directed assembly of 1D π-conjugated peptides on lattice-matched 1D vdW surfaces with enhanced photophysical and optoelectronic properties. We anticipate that this strategy could be translated to the interfacing of an array of π-conjugated peptide-based or organic molecular materials and 1D vdW solids and will fundamentally contribute to the growing understanding of the supramolecular self-assembly on inorganic surfaces.

Results

Here, we test our hypothesis that crystalline 1D vdW inorganic surfaces that display lattice surfaces with atomic spacings that correspond to π-π interaction distances, typically in the range of 3.4 ~ 3.5 Å (*45–47*), can direct the supramolecular assembly of organic optoelectronic π-conjugated molecules (Figure 1A). To demonstrate our synthetic strategy, we utilize a model π-conjugated peptide (DDD-4T) comprised of a central π-conjugated unit of quaterthiophene (4T) and a peptide sequence of three ionizable aspartic acids (DDD) at the periphery of the conjugated core (Figure 1B). Benefiting from the favorable 1D growth and assembly *via* π-π interactions and hydrogen bonds of these supramolecular units, DDD-4T can reliably form 1D chiral nanostructures in aqueous acidic solutions (Figure 1C−F, Figure S1) (*48–50*). The ideality of the model DDD-4T π-conjugated peptide relies on both the attractive semiconducting and optoelectronic properties of high aspect ratio 1D nanostructures formed by peptide-functionalized 4T units, as well as the pH-triggered hydrogen bonding interactions arising from the incorporation of three aspartic acids that reliably facilitate supramolecular 1D growth (*47*, *51–54*). Based on our molecular simulations of the freestanding assembly structures that accounted for 20 molecules of DDD-4T, the typical π-π distances distribute ~3.5 Å (3.46 ± 0.02 Å, average ± standard error of the mean) from molecular simulations (Figure 1C,D). To guide the 1D assembly of these π-conjugated peptides on surfaces, we utilized a model inorganic 1D vdW single crystal in the form of highly crystalline NbS_3 (Figure 1I).

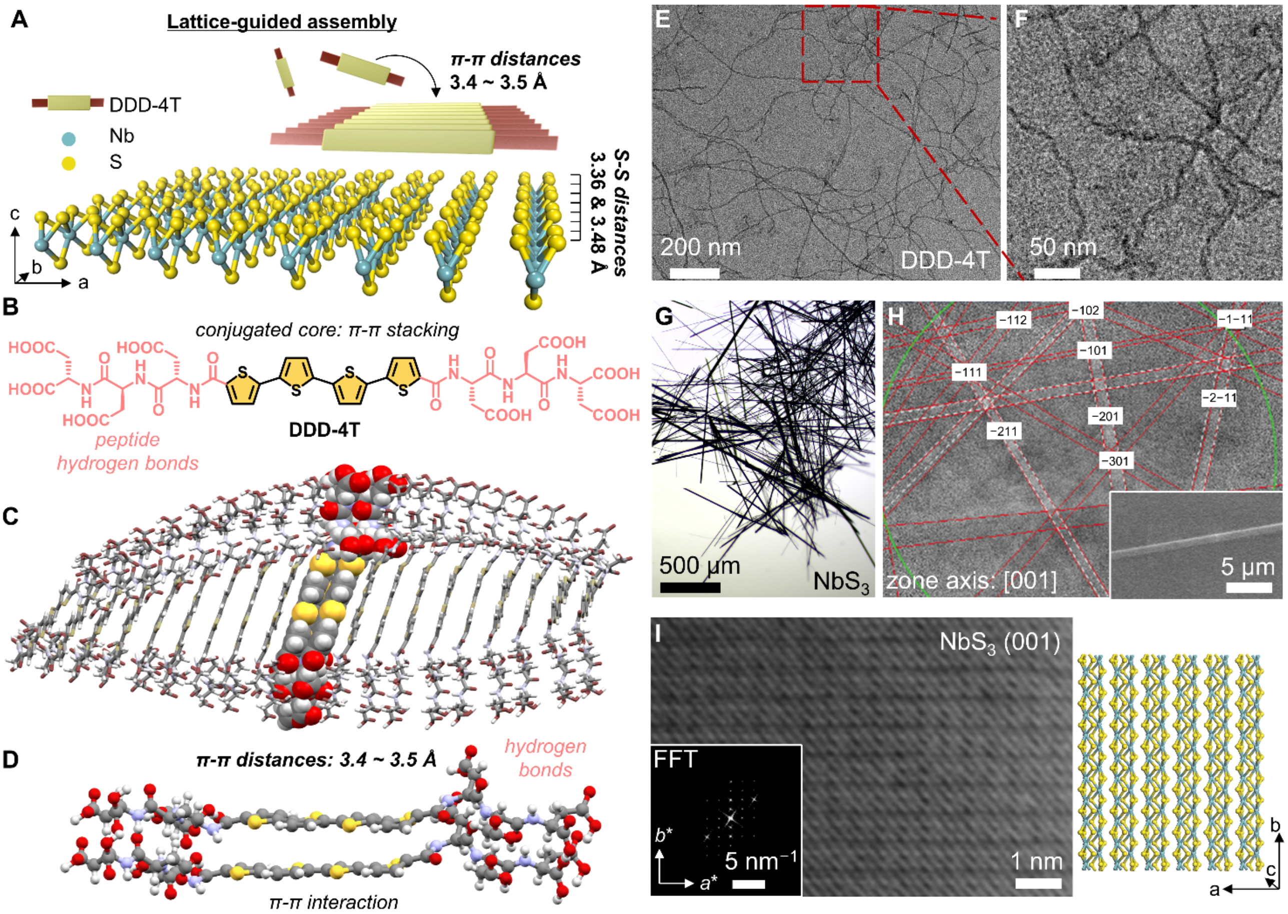

Figure 1. Lattice-guided assembly of π-conjugated peptides on 1D vdW crystal surfaces. (A) Schematic of the directed assembly of DDD-4T on the surface of NbS_3 including the crystal structure representation of the 1D vdW chains of NbS_3 along the (001) surface and the corresponding S-S distances that closely resemble the π-π stacking distances of quaterthiophene (4T) units. (B) Chemical structure of the π-conjugated DDD-4T monomer featuring the 4T core (in yellow) and the peptide backbone (in red). (C) Energy-minimized assembly structures of DDD-4T with 20 molecules. The central dimer unit is projected using a space-filling motif for illustrative purposes. (D) Dimer structure of DDD-4T highlighting the regions of π−π interactions and hydrogen bonding. For C and D, dark gray, light gray, purple, red, and yellow atoms correspond to C, H, N, O, and S atoms, respectively. (E, F) TEM images of acid-triggered solution phase assembly of DDD-4T nanostructures showing the 1D nature of the assemblies. (G) Optical microscopy image of bulk needle-like crystals of NbS_3. (H) EBSD pattern of a micromechanically exfoliated NbS_3 single crystal surface along the [001] zone axis. Inset: corresponding SEM image of the exfoliated crystal. (I) Representative STEM image and FFT of an NbS_3 (001) surface (left) and the directly matched crystal structure model of NbS_3 along the [001] zone axis (right). In the crystal structure representations of NbS_3, teal atoms represent Nb and yellow atoms represent S.

The crystal structure of NbS_3 (Type I) is characterized by a dimerized 1D chain of sulfur-coordinated niobium atoms, resulting in sizeable 1D needle-like morphologies (Figure 1G and Figure S2)

(*31*, *38*, *55*). The periodic sulfur atoms in NbS_3 distribute at distances of 3.36 and 3.48 Å along the [010]-direction (crystallographic *b*-axis) of the (001) surface (Figure 1A and Figure S2), which is very close to the literature and simulated π-π distances for 4T and other π-conjugated units. In this work, specifically, we will test whether the self-assembly of π-conjugated peptides can be guided by the periodic lattice spacing of the NbS_3 (001) surface due to the structural similarity between the idealized stacking distance and lattice periodicity (~3.5 Å). We adopted NbS_3 as the model system to demonstrate the growth of 1D organic-inorganic vdW heterointerfaced assemblies since NbS_3 displays a well-defined and atomically flat surface of sulfur atoms on the vdW (001) surface. The electron backscatter diffraction (EBSD) pattern of a micromechanically exfoliated NbS_3 crystal surface is indexable to the [001] zone axis, supporting the expected 1D structure of NbS_3 as well as the exposed (001) vdW surface that displays the suitable crystallographic orientation that matches the π-π distances of the target monomers (Figure 1H). We further complement the EBSD imaging with scanning transmission electron microscopy (STEM) of NbS_3 crystals which evidently showed the atomically well-resolved structure of the (001) vdW surface and highlighted the underlying 1D chain structure of NbS_3 (Figure 1I). As a reference surface, we also sought to compare the templating efficiency of NbS_3 (001) surface to another 1D vDW crystal, TaS_3. Instead of having an atomically flat sulfur-based surface, the reference TaS_3 crystal is comprised of corrugated 1D chains of sulfur atoms oriented along its (100) surface (Figure S3).

Molecular dynamics (MD) simulations were performed to understand the interactions between the π-conjugated peptide and the 1D vdW crystal surface, as well as to predict the possible assembly structures formed by the π-conjugated peptide monomers. Based on the crystal structure, EBSD imaging, and TEM results, we used the expected vdW surfaces of NbS_3 and TaS_3 that correspond to the (001) and (100) surfaces, respectively (Figure 2A,B and Figure S3). These correspond to the same surface and orientation as the Miller indices only differ due to the axis assignments by convention. The experimental single crystal structures were expanded to 14 × 10 × 1 and 1 × 20 × 5 supercells, respectively, to generate a sufficient lattice surface for adding the assembly structures of 10 molecules (Figure 2C,F and Figure S4). The long-axis (intrachain covalent direction) of NbS_3 and TaS_3 were kept along the *b*-axis. By convention based on the reported crystal structures, the interchain vdW directions were oriented along the *c*-axis and *a*-axis for NbS_3 and TaS_3, respectively. The molecular assemblies were positioned to orient the π-π stacking direction along the intrachain covalent directions, which is the *b*-axis for NbS_3 and TaS_3 crystal structures. A vacuum layer of > 50 Å was then added to eliminate the mirror self-interactions. The resulting DDD-4T/NbS_3 heterointerfaced assembly models were geometrically optimized with the universal force field (UFF) and equilibrated atomic charges (*56*, *57*).

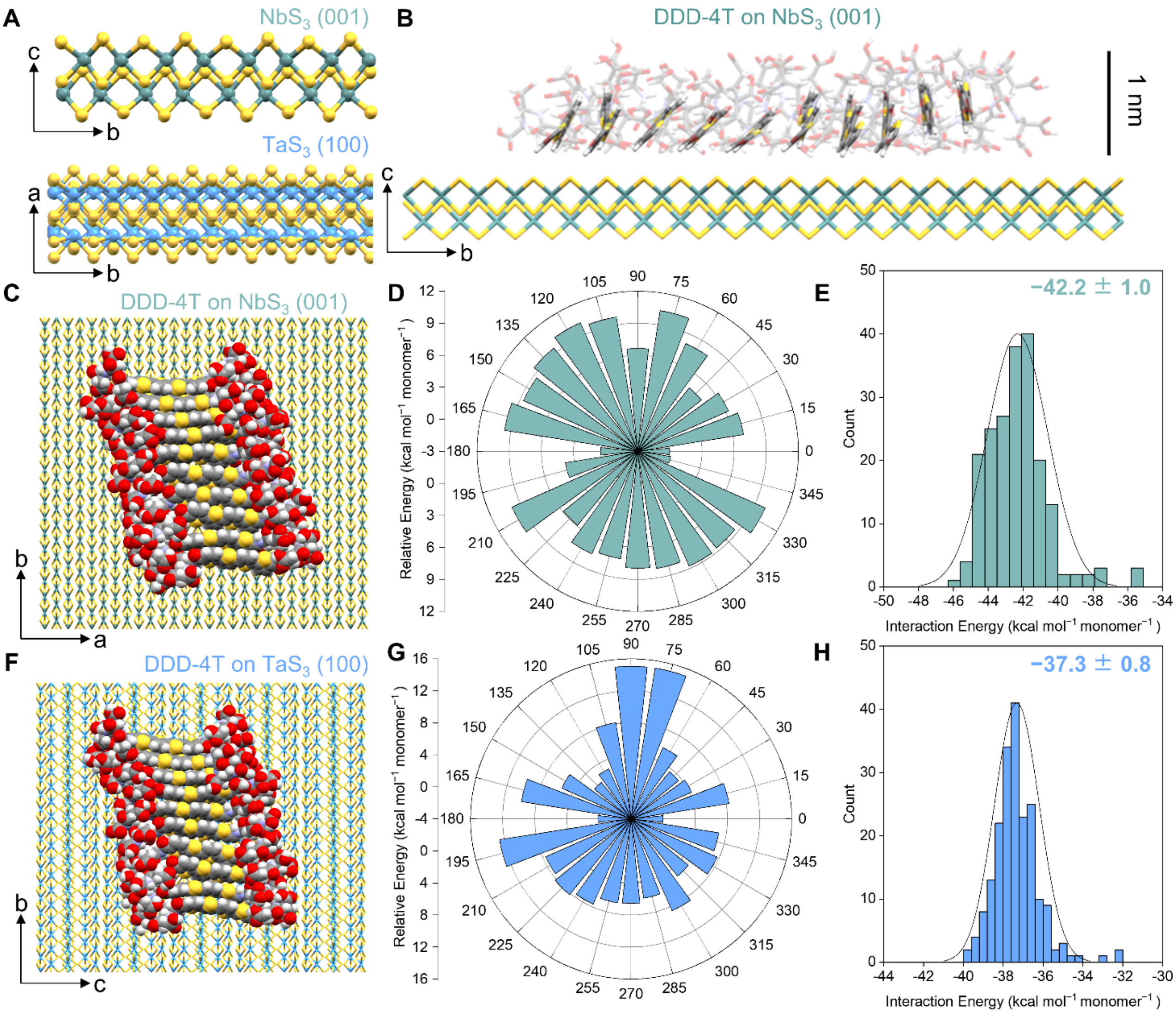

Figure 2. Molecular dynamics simulations of the heterointerfaced assembly structures of DDD-4T on NbS_3 and TaS_3. (A) Side view of the vdW surfaces of NbS_3 (001) and TaS_3 (100). The [001] and [100] directions corresponding to the zone axes of the NbS_3 and TaS_3 surfaces are oriented along the vertical axis. (B) Side view of a representative snapshot of ten molecules of DDD-4T on NbS_3. The other atomic units were made translucent to highlight the correspondence of the opaque 4T units with the NbS_3 surface. Note that the [001] direction corresponding to the zone axis of the NbS_3 surface is oriented along the vertical axis. Top views of the representative snapshot of ten molecules of DDD-4T on (C) NbS_3 (001) and (F) TaS_3 (100) surfaces. For emphases, the DDD-4T molecules were represented as space-filling models. These structures are oriented along the [001] and [100] zone axes corresponding to the NbS_3 and TaS_3 surfaces used in this study, respectively. Distribution of the estimated total energy evolution as the π–π stacking directions were rotated with respect to the (D) NbS_3 and (G) TaS_3 long-axis directions (oriented along 0°/180°). The energetically favorable orientations of the DDD-4T assembly are observed when the

π−π directions are parallel to the NbS_3 or TaS_3 chain directions. Interaction energy histograms between (E) DDD-4T/NbS_3 and (H) DDD-4T/TaS_3 which includes the calculated average and standard error of the mean. In the crystal structure representations of NbS_3 and TaS_3, teal, blue, and yellow atoms represent Nb, Ta, and S atoms, respectively.

The preferential alignment between the π-π interaction distance of DDD-4T units and the intrachain direction of inorganic crystals were assessed by rotating the molecular assemblies every 15° followed by subsequent energy minimizations (Figure S5). We calculated the total energies of heterostructures of DDD-4T assemblies on NbS_3 at different alignment angles (Figure 2D). Generally, the heterostructures showed relatively lower energies when the π-π stacking of the DDD-4T assembly was aligned to the intrachain directions of NbS_3. The lower energies suggest that the DDD-4T molecules would favorably form π-π stacking along the 1D intrachain directions, which suggests that the sulfur atom ordering on the crystal surface could effectively template the molecular assembly of DDD-4T. Furthermore, we estimated the interaction energies from 200 equilibrated MD snapshots with the favorable orientation of molecular assemblies on the crystal surface using the equation of $\Delta E = E_{\mathrm{AB}} - E_{\mathrm{A}} - E_{\mathrm{B}}$, where ΔE is the interaction energy, E_{AB}, E_{A}, and E_{B} are energies of the heterostructure, crystal surface, and peptide assemblies, respectively. The interaction energies of DDD-4T/NbS_3 were estimated to be –42.2 ± 1.0 kcal mol^{-1} per monomer (Figure 2E). These results imply that there could be a direct influence of the underlying NbS_3 surface structure on the self-assembly behavior of the DDD-4T π-conjugated peptides to form 1D-1D organic-inorganic heterointerfaced assemblies. When the MD simulations were performed on the DDD-4T/TaS_3 heterointerface, we also found that the assembly has a lower energy when DDD-4T was oriented along the long-axis direction of the underlying TaS_3 surface (Figure 2G). However, as expected from the corrugated nature of the surface, the interaction energies of the DDD-4T/TaS_3 heterointerface which was estimated at –37.3 ± 0.8 kcal mol^{-1} per monomer was found to be higher as compared to its NbS_3 counterpart (Figure 2H). The lower interaction energy of –42.2 ± 1.0 kcal mol^{-1} per monomer of DDD-4T/NbS_3 is a qualitatively significant energy difference compared with –37.3 ± 0.8 kcal mol^{-1} per monomer of DDD-4T/TaS_3 (*24*, *58*, *59*), suggesting that the π-conjugated peptides would more readily assemble on the NbS_3 surface than TaS_3. This result is supported by the microscopy and spectra shown in the next section.

To probe the assembly behavior of DDD-4T on the surface of 1D vdW crystals, and to experimentally validate our simulations, sizeable single crystals of NbS_3 and TaS_3 were incubated with aqueous solutions of DDD-4T (1 μM, pH 6) (Figure 3A). At pH 6, in consideration of the pK_a of aspartic acid, DDD-4T is expected to still possess negatively charged residues preventing the pre-aggregation of these π-conjugated peptides into high aspect ratio 1D structures prior to interfacing with the 1D vdW surfaces. For these incubation experiments, we implemented two methods that allow for the formation of nucleation sites and the growth of peptides in 1D. To establish a fluorescence baseline from DDD-4T and to confirm that there is no background fluorescence from NbS_3, we show that the DDD-4T solution exhibited homogeneous and weak fluorescence (excitation: 450 – 490 nm; emission: 500 – 550 nm) under microscopy and NbS_3 crystals showed negligible fluorescence within the same wavelength range (Figure S6). We demonstrate the assembly of DDD-4T by incubating the crystals in the DDD-4T solution for 2 – 24 h to allow nucleation and slow growth, followed by the removal of the solution for subsequent natural drying to allow further growth (*Method 1*, Figure 3A). After solution drying, the fluorescence microscopy images clearly showed significantly enhanced, highly localized, and well-ordered fluorescence on NbS_3 (Figure 3B, Figure S7A, and Figure S8) compared to the original crystals and solutions (Figure S6). These results suggest that regions where DDD-4T molecules concentrated to form 1D assemblies on the NbS_3 crystal surface. On the other hand, when the crystals were kept in solution (*Method 2*, Figure 3A), DDD-4T showed slow assembly kinetics to form even longer assemblies on the crystal surface, with some examples reaching lengths of more than 200 µm after a 15-day incubation period (Figure 3C, Figure S7B, and Figure S9). Quantitative integration of the fluorescence microscopy images also supports the different growth rates of DDD-4T assemblies on NbS_3 crystal surfaces (Figure 3E). As expected, although DDD-4T could form assembled arrays on NbS_3, no apparent assemblies were observed on TaS_3 even with the same conditions used in both Methods 1 and 2 (Figure S10). We attribute this to the more positive interaction energies between the DDD-4T and the corrugated TaS_3 surface that hinder the monomeric precursors from overcoming the nucleation energy barrier to form supramolecular assemblies (*60*, *61*).

Atomic force microscopy (AFM) was performed to further gain morphological insights on the DDD-4T assemblies on NbS_3 crystal surfaces. Accordingly, DDD-4T formed 1D ribbon-like nanostructures on NbS_3 crystal surfaces, where the assemblies showed thicknesses of 1.5 ~ 2.0, 1.0 ~ 2.1, and 2.8 ~ 5.1 nm (1.58 ± 0.09, 1.17 ± 0.05, and 4.43 ± 0.53 nm as average with standard error of the mean) for 4, 8, and 24 h incubation, respectively (Figure 3D and Figure S11). As a comparison, bare NbS_3 crystals showed smooth surfaces or multiple crystal edges (Figure S12). The nanometer thickness of DDD-4T assemblies on NbS_3 crystal surfaces indicates several molecular layers, while one molecular layer is around 1 nm (Figure 2B). Furthermore, the longitudinal direction of molecular assemblies followed the long-axis direction of NbS_3 1D crystals, which is in accordance with the simulated direction from MD calculations (Figure 2D). It is particularly interesting to note the flat nature of the DDD-4T assembly on the NbS_3 surface which is in stark contrast to its typical freestanding twisted/helical morphology when assembled in solution.

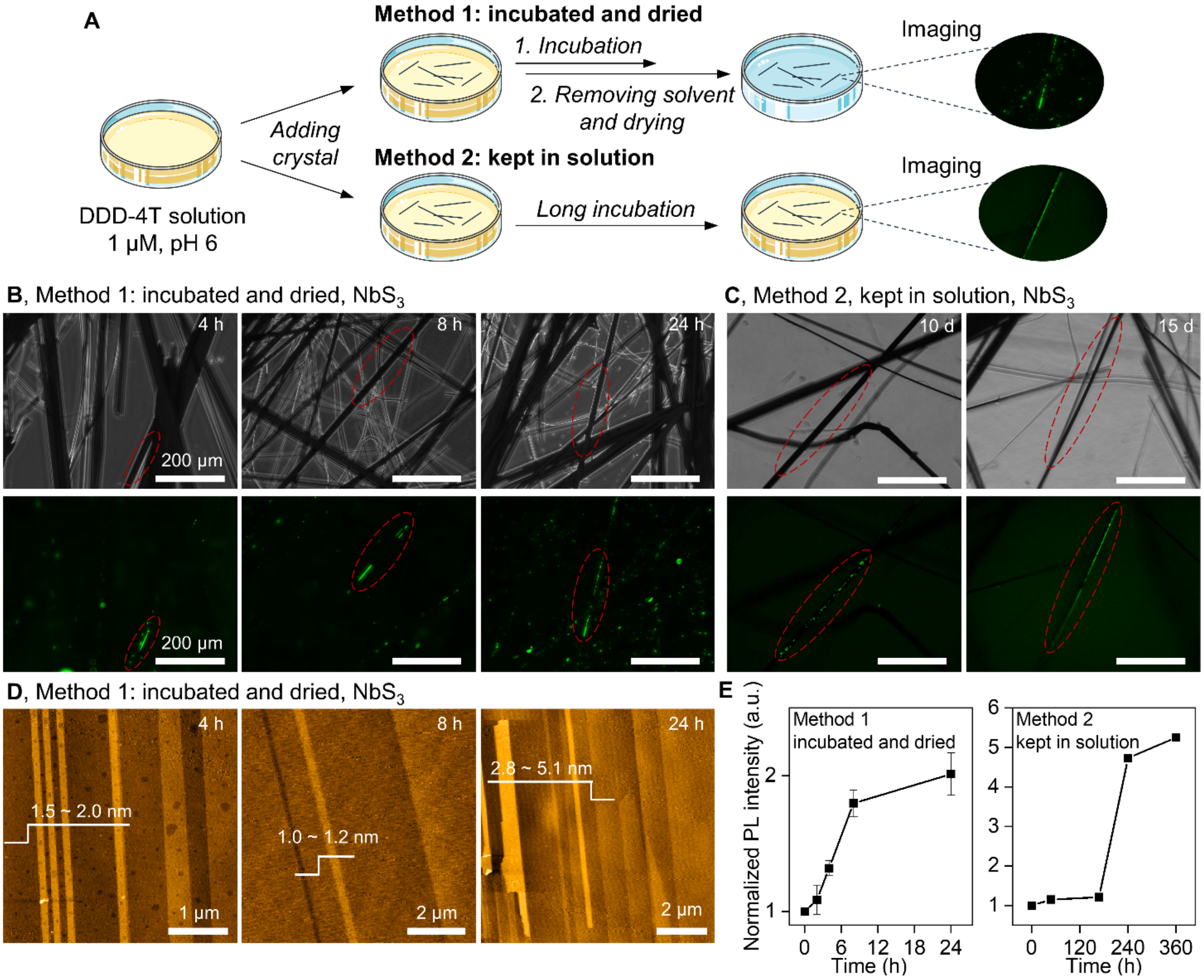

Figure 3. Time-dependent evolution of DDD-4T assembly on the NbS_3 crystal surface. (A) Schematic diagram of two growth methods used in this study. A portion of this figure was created with BioRender.com. (B) Representative brightfield (top row) and fluorescence (bottom row) microscopy images of the NbS_3 crystals after incubation with the DDD-4T monomer solution (1 µM, pH 6) at specific time points. The samples were naturally dried in air prior to imaging. (C) Representative brightfield (top row) and fluorescence (bottom row) microscopy images of the NbS_3 crystals after incubation with the DDD-4T monomer solution (1 µM, pH 6) at specific time points. The samples were kept in solution during imaging. All scale bars in (B) and (C) are 200 µm. All fluorescence microscopy images were obtained with excitation of 450 – 490 nm and emission of 500 – 550 nm. (D) AFM height images of the DDD-4T assemblies on NbS_3 crystal with corresponding step heights indicated. The corresponding height profiles can be found in Figure S11. (E) Relative evolution of the fluorescence intensity (average with standard error of the mean) as a function of incubation time of the DDD-4T monomers on the NbS_3 crystal surface. The fluorescence intensities are calculated from the fluorescence microscopy images and normalized to the initial value before incubation.

The well-defined morphologies of assembled DDD-4T on the surface of NbS_3 enabled us to systematically probe the influence of surface assembly on the physical properties of DDD-4T. To investigate the molecular ordering at the interface of DDD-4T/NbS_3 heterostructures, we performed photoluminescence and Raman mapping on an NbS_3 crystal incubated with the DDD-4T monomer solution (pH ~6) for 8 h (Figure 4). The prominent false-color fluorescence arising from 470 nm excitation wavelength verified the assembly of DDD-4T on the NbS_3 crystal surface (Figure 4A). We then mapped the same area using the photoluminescence (PL) signal from DDD-4T (405 nm laser line) and Raman phonon mode signals from NbS_3 (167 – 240 cm^{-1}; 532 nm laser line) obtained from rastering the laser beam in a micro-Raman spectrometer (Figure 4B). These spatial conformity of both the PL signal and the Raman map to the expected deposition regions confirm the assembly of DDD-4T on the crystal surface. The PL spectral profile of DDD-4T on NbS_3 showed multiple peaks that signify various intrinsic vibronic modes. Upon inspection, we observe that the aggregated PL peaks red-shifted by approximately 50 to 70 nm compared to DDD-4T in solution or on SiO_2 substrates, assembled at pH 2 and 6, respectively (Figure 4E, Figure S13). The significant red shift suggests that the 4T chromophores of DDD-4T manifest more pronounced intermolecular interactions, thereby leading to a stronger polarization effect to lower the energy of excited state in the aggregates. We found that these observations closely resemble the red-shifting of photoluminescence peaks observed in reports that depict ordered quaterthiophene aggregates (*62–64*). Like in prior described samples (Figure 3D and Figure S11), AFM imaging of these mapping regions revealed 1D assemblies of DDD-4T with a thickness of 0.8 ~ 1.2 nm on the same NbS_3 crystals (Figure 4F). Unlike the twisted 1D nanostructures with evident entanglements induced by acid-triggered assembly in solution (Figure 1H,I and Figure 4G), the DDD-4T assemblies on NbS_3 crystals presented a more uniform flat morphology, devoid of twisted features, looping, or entanglements (Figure 4F, Figure 3D, and Figure S11). Our MD simulations suggested that the NbS_3 crystal surface can significantly adsorb DDD-4T molecules in a structurally templated manner (Figure 2), which could lead to considerably untwisted molecular packing structures.

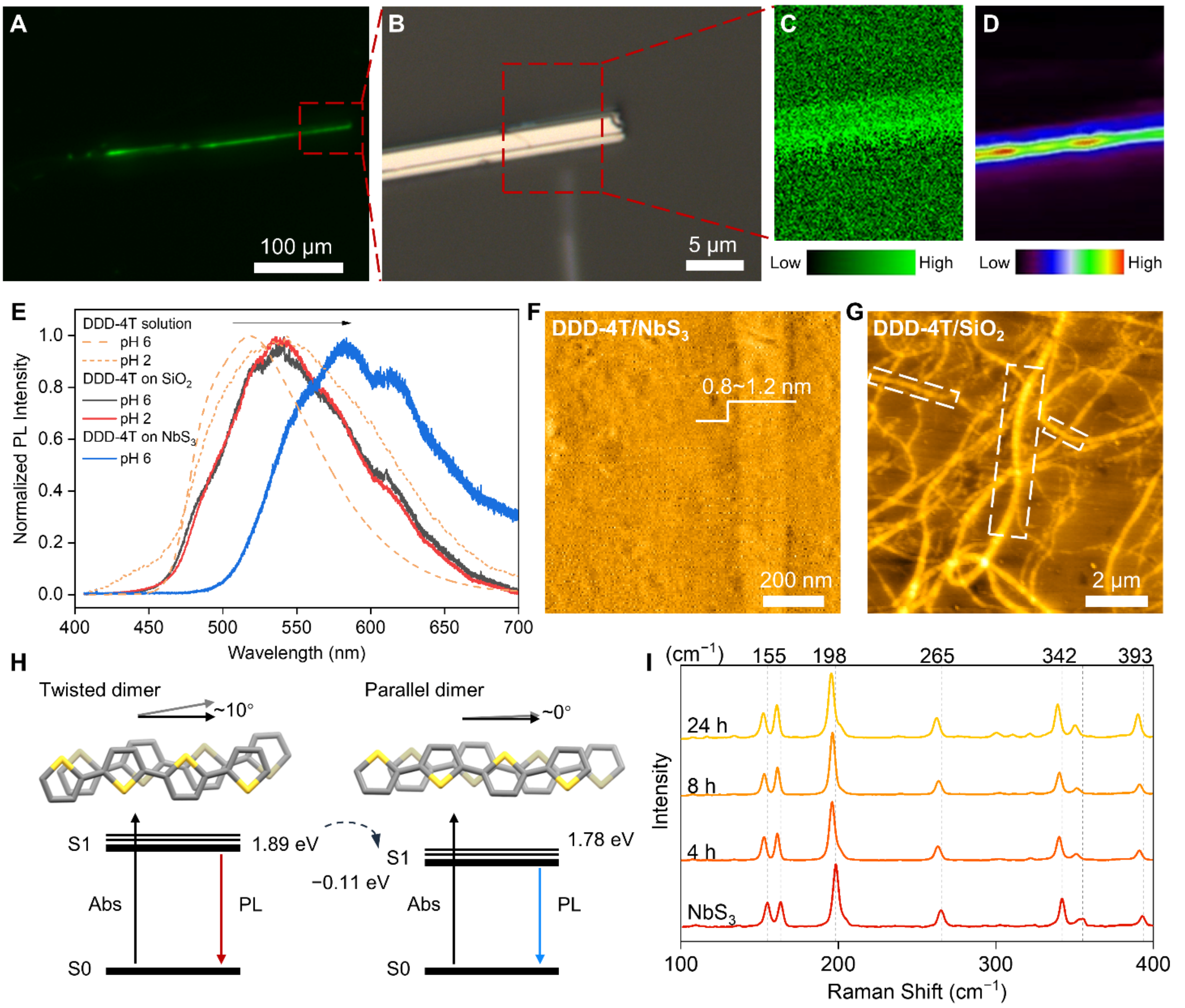

Figure 4. Spectroscopic characterization of the DDD-4T/NbS$_3$ heterointerfaced assemblies. (A) Fluorescence image of a NbS$_3$ crystal after incubation with the DDD-4T solution (1 μM, pH 6) for 8 h followed by air drying (Method 1). The red dashed frame highlights the imaging region of interest. (B) Corresponding brightfield optical image of the region of interest of the NbS$_3$ crystal with the assembled DDD-4T. The red dashed frame indicated mapping region in C and D. (C) Raman mapping based on the phonon signals from NbS$_3$ (167 – 240 cm^{-1} region, excitation: 532 nm). (D) Photoluminescence mapping based on the PL signals from DDD-4T (417 – 423 nm region, excitation: 405 nm). This specific region was selected to maximize the integrable signal without saturating the detector during the PL mapping. (E) Photoluminescence profiles of DDD-4T on SiO$_2$ substrates or NbS$_3$ after incubation with DDD-4T solution (1 μM, pH 2 or 6) for 8 h followed by air drying (Method 1). (F) Representative AFM height image of the DDD-4T/NbS$_3$ heterointerface corresponding to the regions imaged and mapped in A-D. (G) Representative AFM height images of the solution phase acid-triggered assemblies of DDD-4T that were dropcasted on SiO$_2$ substrates. Three white dashed frames were included as guides to the eye and highlight the 1D twisted nanostructure formed from solution. (H) Energy-minimized structures of twisted or parallel 4T dimers and corresponding TDDFT-calculated energies of the excited states. The peptide sidechains were omitted for ease of calculation. (I)

Raman spectra of the NbS_3 crystal and the DDD-4T/NbS_3 heterointerfaced assemblies showing the influence of DDD-4T deposition on NbS_3 phonon modes (excitation: 532 nm).

To further reconcile the morphological observation and recorded photophysical properties, we performed time-dependent density functional theory (TDDFT) calculations on stacked dimer of quaterthiophenes (*63*, *65*). Using MD simulated structures, we optimized two idealized dimer models with different twisted angles of approximately 0° (close to the molecules on the substrate) and 10° (close to the molecules in solution) (Figure 4H). The twisted dimer structure exhibited a larger optical gap of 1.89 eV between the ground (S_0) and excited states (S_1) compared to the untwisted dimer structure. This disparity is also consistent with previously reported for the twisted dimer of another π-conjugated unit (perylene diimide) (*66*). To complement these results, we conducted Raman spectral analysis on the DDD-4T/NbS_3 heterointerfaces to assess the direct influence of DDD-4T deposition on the lattice vibrations of NbS_3. The Raman peaks at ~155 (Peaks 1 and 2), 198 (Peak 3), 265 (Peak 4), 342 (Peak 5 and 6), and 393 (Peak 7) cm^{-1} are assignable to the lattice compression along the chain and Nb-Nb stretching modes (Peaks 1 and 2), Nb-S_2 vibrational mode (Peak 3), symmetrical valence of the Nb-S vibrational mode (Peak 4), intrachain Nb-S vibrational modes (Peaks 5 and 6), and interchain Nb-S vibrational modes (Peak 7), respectively (Figure 4I and Figure S14) (*67*). As the incubation time increased from 0 to 24 h, these calibrated Raman peaks shifted to lower wavenumbers by 2–4 cm^{-1} (Figure 4I and Figure S14), indicating a slight overall lattice expansion within the NbS_3 lattice upon the assembly of DDD-4T on the crystal surface.

Lastly, we demonstrate the functional impact of the lattice-guided formation of organic-inorganic heterointerfaces between the π-conjugated peptides and 1D vdW crystals that we present herein by quantifying the degree of photocurrent generation in prototype devices (Figure 5). Heterostructures comprising of conjugated molecules on 2D materials have been shown to manifest promising potential as photoconductive materials (*68*–*70*). To measure the influence of the templating strategy on the optoelectronic activity of the resulting materials, the photocurrent generating ability of the DDD-4T/NbS_3 heterointerfaced assembly was compared to the dropcasted film of π-conjugated peptides obtained *via* acid-triggered assembly in solution by fabricating Ag-contacted two-probe devices based on these two distinct samples (Figure 5A,B). The DDD-4T/NbS_3 heterointerfaced assembly device was prepared by incubating pre-contacted NbS_3 crystal devices with the DDD-4T monomer solution for 8 h, followed by removing the solution and natural air-drying. In these devices, the apparent well-defined fluorescence of DDD-4T concentrated on the crystal surface verified the formation of DDD-4T assemblies

(Figure 5C). NbS_3, a known indirect gap semiconductor (*42*, *71*, *72*), exhibited a measured conductivity of 1.28 ± 0.03 S cm^{-1} in the fabricated crystal device (Figure 5D), resulting in a measurable current of approximately 750 nA at 10 V. Meanwhile, the dropcasted film derived from acid-triggered solution phase assembly of DDD-4T was confirmed to show uniform fluorescence (Figure S15) and measured conductivities of 0.015 ± 0.002 S cm^{-1} (Figure 5D). Notably, when the DDD-4T is assembled on the surface of NbS_3 to form the DDD-4T/NbS_3 heterointerfaced assembly was measured, the device exhibited photocurrents of about 2.40 ± 0.06 nA upon illumination with a 415-nm LED light source at an intensity of 16 mW cm^{-2} (Figure 5E,F and Figure S16). Based on these measurements, we calculated a photocurrent density of 9.9 ± 0.2 μA cm^{-2} by normalizing the measured photocurrent to the device area (Figure 5F). This photocurrent generation behavior upon visible light excitation (415 nm) was consistent with another individually fabricated device incubated with DDD-4T which yielded measured photocurrents of approximately 2.0 nA under the same illumination conditions (Figure S16). Moreover, the DDD-4T/NbS_3 heterostructure device exhibited substantial responsiveness to light pulse frequencies of 1 and 2 Hz. In comparison, the NbS_3 crystal-based control device showed no noticeable photocurrent before the deposition of the DDD-4T molecules under the experimental conditions (*42*, *71*, *72*). Additionally, the drop-coated thin film control device based on solution-assembled DDD-4T exhibited significantly weaker photocurrents of about 0.084 ± 0.004 nA and a photocurrent density of 0.17 ± 0.01 μA cm^{-2} (Figure 5E,F). Overall, these prototypical device measurements underscore the enhancement of photocurrent generation in DDD-4T/NbS_3 heterostructures, reaching up to about ~58 times increase of photocurrent density compared to the individual DDD-4T assembled film (Figure 5F). Based on these measurements, we infer that the enhanced photocurrent generation is, in greater part, due to the efficient collection of the photogenerated carriers from DDD-4T into the significantly more conducting NbS_3 crystal. The demonstrated photocurrent enhancement suggests the improved molecular ordering of π-conjugated peptides at the interface, providing potential applications as photodetectors and sensors based on organic-inorganic heterostructures (*22*, *23*, *73*).

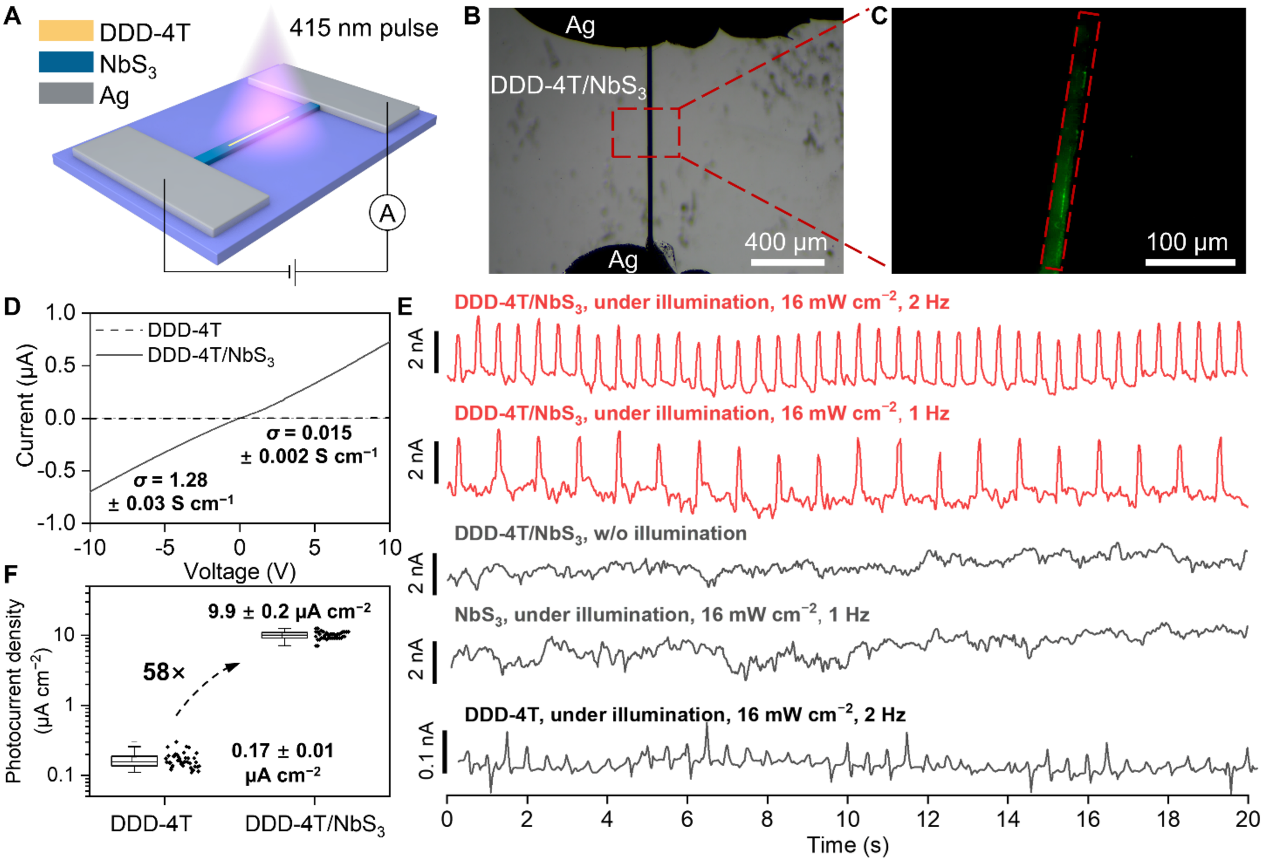

Figure 5. Enhanced photocurrent generation in DDD-4T/NbS_3 heterointerfaced assemblies. (A) Schematic diagram of the photocurrent-generating prototype device based on the DDD-4T/NbS_3 heterointerfaced assembly. (B) Optical microscopy image of the DDD-4T/NbS_3 device depicting the positioning of the assembly with respect to the Ag electrodes. (C) Fluorescence microscopy image of the assembled DDD-4T on the surface of the NbS_3 crystal depicted in B. The red dashed frames in B and C highlight the imaged crystal region. (D) Current−voltage curves of the DDD-4T/NbS_3 heterointerfaced assembly device and the solution-assembled DDD-4T dropcasted thin film control device. (E) Current−time curves depicting photocurrent generation of the DDD-4T/NbS_3 heterointerfaced assembly, control NbS_3, and solution-assembled DDD-4T dropcasted thin film control device under illumination (415 nm, 16 mW cm^{-2}). (F) Pronounced enhancement of the photocurrent density in the DDD-4T heterointerfaced assembly device in comparison with the solution-assembled DDD-4T dropcasted thin film control device. The photocurrent density values were measured using the 40 peaks derived from the Current−time curves in (E). These curves were measured with 2 Hz illumination and were normalized with the device area (DDD-4T/NbS_3 heterointerfaced assembly device: 23 μm × 1053 μm; solution-assembled DDD-4T dropcasted thin film control device: 500 μm × 100 μm).

Discussion

In this study, we presented a lattice-guided strategy towards creating optoelectronically active 1D heterointerface of organic π-conjugated peptides and inorganic 1D vdW crystals of NbS_3. The periodic distribution of sulfur atoms on the NbS_3 (001) crystal surfaces served as a suitable interfacial assembly template for the π-π interactions within the peptidic supramolecular assemblies, which typically exhibit distances of around 3.5 Å. We have observed that the π-conjugated peptides could self-organize on 1D vdW crystal interfaces into highly ordered 1D assembly structures, which is morphologically flat and straight—distinct from the acid-triggered twisted assemblies. The lattice-guided assembly of π-conjugated peptides on NbS_3 crystals is well supported by various experimental characterizations and computational simulations that we have shown throughout the study. Moreover, the DDD-4T/NbS_3 heterointerfaced assemblies displayed markedly improved photocurrent generation upon excitation with 415 nm light pulses. In particular, the heterointerfaced assemblies exhibited an enhancement in photocurrent density up to 9.9 ± 0.2 µA cm^{-2}, which is ~58 times higher compared to the solution-assembled DDD-4T dropcasted thin film control device. Collectively, our work presents a means towards creating well-defined organic-inorganic assemblies endowed with photocurrent generation capability under visible light, offering proof-of-concept insights on the directed self-assembly pathways that enable the optoelectronic functionality of these heterointerfaced assemblies.

Supplementary Materials

The Supporting Materials document is available free of charge including material and method descriptions and additional figures.

Acknowledgments

This work was supported by the University of California, Irvine (UCI). We also acknowledge partial support by the National Heart, Lung, And Blood Institute (NHLBI) of the National Institutes of Health (NIH) under Award Number 1R56HL164348-01. The content is solely the responsibility of the authors and does not necessarily represent the official views of the National Institutes of Health. The authors acknowledge the use of facilities and instrumentation at the UC Irvine Materials Research Institute (IMRI), which is supported, in part, by the National Science Foundation Materials Research Science and Engineering Center: Center for Complex and Active Materials (DMR-2011967). The authors acknowledge the Research Cyberinfrastructure Center (RCIC) at UCI for supporting the computational work. AFM was performed using an Anton Paar Tosca 400 AFM on loan to IMRI from Anton Paar GmbH. The authors also thank Dr. Dmitry Fishman for the access to equipment in the UC Irvine Department of Chemistry Laser Spectroscopy Laboratories.

Author contributions

Conceptualization: HAMA, MQA

Methodology: ZFY, HAMA, MQA

Investigation: ZFY, DLMC, GMM, DL, SJA, YK

Visualization: ZFY

Funding acquisition: HAMA, MQA

Project administration: HAMA, MQA

Supervision: HAMA, MQA

Writing – original draft: ZFY, HAMA, MQA

Writing – review & editing: ZFY, DLMC, GMM, DL, SJA, YK, HAMA, MQA

* HAMA and MQA are co-corresponding authors

Competing interests

The authors declare that they have no competing interests.

References

1. J. Cornil, D. Beljonne, J.-P. Calbert, J.-L. Brédas, Interchain Interactions in Organic π-Conjugated Materials: Impact on Electronic Structure, Optical Response, and Charge Transport. *Adv. Mater.* **13**, 1053–1067 (2001).
2. F. Würthner, C. R. Saha-Möller, B. Fimmel, S. Ogi, P. Leowanawat, D. Schmidt, Perylene Bisimide Dye Assemblies as Archetype Functional Supramolecular Materials. *Chem. Rev.* **116**, 962–1052 (2016).
3. M. F. J. Mabesoone, A. R. A. Palmans, E. W. Meijer, Solute–Solvent Interactions in Modern Physical Organic Chemistry: Supramolecular Polymers as a Muse. *J. Am. Chem. Soc.* **142**, 19781–19798 (2020).
4. L. Adler-Abramovich, E. Gazit, The physical properties of supramolecular peptide assemblies: From building block association to technological applications. *Chem. Soc. Rev.* **43**, 6881–6893 (2014).
5. F. Sheehan, D. Sementa, A. Jain, M. Kumar, M. Tayarani-Najjaran, D. Kroiss, R. V. Ulijn, Peptide-Based Supramolecular Systems Chemistry. *Chem. Rev.* **121**, 13869–13914 (2021).

6. T. Aida, E. W. Meijer, S. I. Stupp, Functional Supramolecular Polymers. *Science*. **335**, 813–817 (2012).
7. K. Tao, P. Makam, R. Aizen, E. Gazit, Self-assembling peptide semiconductors. *Science*. **358**, eaam9756 (2017).
8. V. Coropceanu, J. Cornil, D. A. da Silva Filho, Y. Olivier, R. Silbey, J.-L. Brédas, Charge Transport in Organic Semiconductors. *Chem. Rev.* **107**, 926–952 (2007).
9. G. Gryn'ova, K.-H. Lin, C. Corminboeuf, Read between the Molecules: Computational Insights into Organic Semiconductors. *J. Am. Chem. Soc.* **140**, 16370–16386 (2018).
10. T. Steiner, S. Thomas, The Hydrogen Bond in the Solid State. *Angew. Chem. Int. Ed.* **41**, 48–76 (2002).
11. J. W. Colson, A. R. Woll, A. Mukherjee, M. P. Levendorf, E. L. Spitler, V. B. Shields, M. G. Spencer, J. Park, W. R. Dichtel, Oriented 2D Covalent Organic Framework Thin Films on Single-Layer Graphene. *Science*. **332**, 228–231 (2011).
12. C. Wang, Q. He, U. Halim, Y. Liu, E. Zhu, Z. Lin, H. Xiao, X. Duan, Z. Feng, R. Cheng, N. O. Weiss, G. Ye, Y.-C. Huang, H. Wu, H.-C. Cheng, I. Shakir, L. Liao, X. Chen, W. A. Goddard III, Y. Huang, X. Duan, Monolayer atomic crystal molecular superlattices. *Nature*. **555**, 231–236 (2018).
13. Y. Liu, Y. Huang, X. Duan, Van der Waals integration before and beyond two-dimensional materials. *Nature*. **567**, 323–333 (2019).
14. J. Sun, Y. Choi, Y. J. Choi, S. Kim, J.-H. Park, S. Lee, J. H. Cho, 2D–Organic Hybrid Heterostructures for Optoelectronic Applications. *Adv. Mater.* **31**, 1803831 (2019).
15. H. Yan, S. H. Park, G. Finkelstein, J. H. Reif, T. H. LaBean, DNA-Templated Self-Assembly of Protein Arrays and Highly Conductive Nanowires. *Science*. **301**, 1882–1884 (2003).
16. J. D. Le, Y. Pinto, N. C. Seeman, K. Musier-Forsyth, T. A. Taton, R. A. Kiehl, DNA-templated self-assembly of metallic nanocomponent arrays on a surface. *Nano Lett.* **4**, 2343–2347 (2004).
17. Y. Lin, A. Böker, J. He, K. Sill, H. Xiang, C. Abetz, X. Li, J. Wang, T. Emrick, S. Long, Q. Wang, A. Balazs, T. P. Russell, Self-directed self-assembly of nanoparticle/copolymer mixtures. *Nature*. **434**, 55–59 (2005).
18. Z.-F. Yao, E. Lundqvist, Y. Kuang, H. A. M. Ardoña, Engineering Multi-Scale Organization for Biotic and Organic Abiotic Electroactive Systems. *Adv. Sci.* **10**, 2205381 (2023).
19. T. R. Kafle, B. Kattel, P. Yao, P. Zereshki, H. Zhao, W.-L. Chan, Effect of the Interfacial Energy Landscape on Photoinduced Charge Generation at the ZnPc/MoS_2 Interface. *J. Am. Chem. Soc.* **141**, 11328–11336 (2019).

20. L. Ye, X. Xu, S. He, Y. Liu, Y. Jin, Y. M. Yang, H. Zhu, Molecular Triplet Sensitization of Monolayer Semiconductors in 2D Organic/Inorganic Hybrid Heterostructures. *ACS Nano*. **16**, 12532–12540 (2022).
21. L. Zhang, A. Sharma, Y. Zhu, Y. Zhang, B. Wang, M. Dong, H. T. Nguyen, Z. Wang, B. Wen, Y. Cao, B. Liu, X. Sun, J. Yang, Z. Li, A. Kar, Y. Shi, D. Macdonald, Z. Yu, X. Wang, Y. Lu, Efficient and Layer-Dependent Exciton Pumping across Atomically Thin Organic-Inorganic Type-I Heterostructures. *Adv. Mater.* **30**, 1803986 (2018).
22. X. Xu, Z. Lou, S. Cheng, P. C. Y. Chow, N. Koch, H.-M. Cheng, Van der Waals organic/inorganic heterostructures in the two-dimensional limit. *Chem*. **7**, 2989–3026 (2021).
23. J. Khan, R. T. M. Ahmad, J. Tan, R. Zhang, U. Khan, B. Liu, Recent advances in 2D organic−inorganic heterostructures for electronics and optoelectronics. *SmartMat*. **4**, 1–32 (2023).
24. J. Chen, E. Zhu, J. Liu, S. Zhang, Z. Lin, X. Duan, H. Heinz, Y. Huang, J. J. De Yoreo, J. J. De Yoreo, Building two-dimensional materials one row at a time: Avoiding the nucleation barrier. *Science*. **362**, 1135–1139 (2018).
25. A. Shi, T. A. Villarreal, A. Singh, T. R. Hayes, T. C. Davis, J. T. Brooks, S. A. Claridge, Plenty of Room at the Top: A Multi-Scale Understanding of nm-Resolution Polymer Patterning on 2D Materials. *Angew. Chem. Int. Ed.* **60**, 25436–25444 (2021).
26. A. Singh, J. C. Arango, A. Shi, J. B. D'Aliberti, S. A. Claridge, Surface-Templated Glycopolymer Nanopatterns Transferred to Hydrogels for Designed Multivalent Carbohydrate–Lectin Interactions across Length Scales. *J. Am. Chem. Soc.* **145**, 1668–1677 (2023).
27. H. B. Balch, A. M. Evans, R. R. Dasari, H. Li, R. Li, S. Thomas, D. Wang, R. P. Bisbey, K. Slicker, I. Castano, S. Xun, L. Jiang, C. Zhu, N. Gianneschi, D. C. Ralph, J.-L. Brédas, S. R. Marder, W. R. Dichtel, F. Wang, Electronically Coupled 2D Polymer/MoS_2 Heterostructures. *J. Am. Chem. Soc.* **142**, 21131–21139 (2020).
28. A. A. Balandin, F. Kargar, T. T. Salguero, R. K. Lake, One-dimensional van der Waals quantum materials. *Mater. Today*. **55**, 74–91 (2022).
29. A. Patra, C. S. Rout, Anisotropic quasi-one-dimensional layered transition-metal trichalcogenides: synthesis, properties and applications. *RSC Adv.* **10**, 36413–36438 (2020).
30. Y. Zhu, D. A. Rehn, E. R. Antoniuk, G. Cheon, R. Freitas, A. Krishnapriyan, E. J. Reed, Spectrum of Exfoliable 1D van der Waals Molecular Wires and Their Electronic Properties. *ACS Nano*. **15**, 9851–9859 (2021).
31. M. Chen, L. Li, M. Xu, W. Li, L. Zheng, X. Wang, Quasi-One-Dimensional van der Waals Transition Metal Trichalcogenides. *Research*. **6**, 0066 (2023).

32. C. Lin, M. Ochi, R. Noguchi, K. Kuroda, M. Sakoda, A. Nomura, M. Tsubota, P. Zhang, C. Bareille, K. Kurokawa, Y. Arai, K. Kawaguchi, H. Tanaka, K. Yaji, A. Harasawa, M. Hashimoto, D. Lu, S. Shin, R. Arita, S. Tanda, T. Kondo, Visualization of the strain-induced topological phase transition in a quasi-one-dimensional superconductor $TaSe_3$. *Nat. Mater.* **20**, 1093–1099 (2021).
33. H. Hatada, M. Nakamura, M. Sotome, Y. Kaneko, N. Ogawa, T. Morimoto, Y. Tokura, M. Kawasaki, Defect tolerant zero-bias topological photocurrent in a ferroelectric semiconductor. *Proc. Natl. Acad. Sci.* **117**, 20411–20415 (2020).
34. N. Shumiya, M. S. Hossain, J.-X. Yin, Z. Wang, M. Litskevich, C. Yoon, Y. Li, Y. Yang, Y.-X. Jiang, G. Cheng, Y.-C. Lin, Q. Zhang, Z.-J. Cheng, T. A. Cochran, D. Multer, X. P. Yang, B. Casas, T.-R. Chang, T. Neupert, Z. Yuan, S. Jia, H. Lin, N. Yao, L. Balicas, F. Zhang, Y. Yao, M. Z. Hasan, Evidence of a room-temperature quantum spin Hall edge state in a higher-order topological insulator. *Nat. Mater.* **21**, 1111–1115 (2022).
35. R. Noguchi, T. Takahashi, K. Kuroda, M. Ochi, T. Shirasawa, M. Sakano, C. Bareille, M. Nakayama, M. D. Watson, K. Yaji, A. Harasawa, H. Iwasawa, P. Dudin, T. K. Kim, M. Hoesch, V. Kandyba, A. Giampietri, A. Barinov, S. Shin, R. Arita, T. Sasagawa, T. Kondo, A weak topological insulator state in quasi-one-dimensional bismuth iodide. *Nature*. **566**, 518–522 (2019).
36. G. Liu, S. Rumyantsev, M. A. Bloodgood, T. T. Salguero, M. Shur, A. A. Balandin, Low-Frequency Electronic Noise in Quasi-1D $TaSe_3$ van der Waals Nanowires. *Nano Lett.* **17**, 377–383 (2017).
37. D. L. M. Cordova, K. Chua, R. M. Huynh, T. Aoki, M. Q. Arguilla, Anisotropy-Driven Crystallization of Dimensionally Resolved Quasi-1D Van der Waals Nanostructures. *J. Am. Chem. Soc.* (2023), doi:10.1021/jacs.3c05887.
38. S. Conejeros, B. Guster, P. Alemany, J.-P. Pouget, E. Canadell, Rich Polymorphism of Layered NbS 3. *Chem. Mater.* **33**, 5449–5463 (2021).
39. D. W. Bullett, Variation of electronic properties with structure of transition metal trichalcogenides. *J. Phys. C Solid State Phys.* **12**, 277–281 (1979).
40. M. D. Randle, A. Lipatov, I. Mansaray, J. E. Han, A. Sinitskii, J. P. Bird, Collective states and charge density waves in the group IV transition metal trichalcogenides. *Appl. Phys. Lett.* **118** (2021), doi:10.1063/5.0052295.
41. S. Hou, Z. Guo, J. Yang, Y. Liu, W. Shen, C. Hu, S. Liu, H. Gu, Z. Wei, Birefringence and Dichroism in Quasi-1D Transition Metal Trichalcogenides: Direct Experimental Investigation. *Small*. **17**, 1–8 (2021).
42. Y. Wang, P. Wu, Z. Wang, M. Luo, F. Zhong, X. Ge, K. Zhang, M. Peng, Y. Ye, Q. Li, H. Ge, J.

Ye, T. He, Y. Chen, T. Xu, C. Yu, Y. Wang, Z. Hu, X. Zhou, C. Shan, M. Long, P. Wang, P. Zhou, W. Hu, Air-Stable Low-Symmetry Narrow-Bandgap 2D Sulfide Niobium for Polarization Photodetection. *Adv. Mater.* **32**, 2005037 (2020).

43. E. V. Formo, J. A. Hachtel, Y. Ghafouri, M. A. Bloodgood, T. T. Salguero, Thermal Stability of Quasi-1D NbS 3 Nanoribbons and Their Transformation to 2D NbS_2: Insights from in Situ Electron Microscopy and Spectroscopy. *Chem. Mater.* **34**, 279–287 (2022).
44. B. Dusabe, G. M. Dongho-Nguimdo, D. P. Joubert, Pressure effect on structural stability and optical absorption of triclinic NbS_3 from DFT and many-body perturbation calculations. *Eur. Phys. J. B*. **93**, 122 (2020).
45. Z. Chen, A. Lohr, C. R. Saha-Möller, F. Würthner, Self-assembled π-stacks of functional dyes in solution: Structural and thermodynamic features. *Chem. Soc. Rev.* **38**, 564–584 (2009).
46. C. Sutton, C. Risko, J.-L. Brédas, Noncovalent Intermolecular Interactions in Organic Electronic Materials: Implications for the Molecular Packing vs Electronic Properties of Acenes. *Chem. Mater.* **28**, 3–16 (2016).
47. Z.-F. Yao, J.-Y. Wang, J. Pei, Control of π–π Stacking via Crystal Engineering in Organic Conjugated Small Molecule Crystals. *Cryst. Growth Des.* **18**, 7–15 (2018).
48. H. A. M. Ardoña, K. Besar, M. Togninalli, H. E. Katz, J. D. Tovar, Sequence-dependent mechanical, photophysical and electrical properties of π-conjugated peptide hydrogelators. *J. Mater. Chem. C*. **3**, 6505–6514 (2015).
49. Z.-F. Yao, Y. Kuang, P. Kohl, Y. Li, H. A. M. Ardoña, Carbodiimide-Fueled Assembly of π-Conjugated Peptides Regulated by Electrostatic Interactions. *ChemSystemsChem*. **5**, e202300003 (2023).
50. T. S. Kale, H. A. M. Ardoña, A. Ertel, J. D. Tovar, Torsional Impacts on Quaterthiophene Segments Confined within Peptidic Nanostructures. *Langmuir*. **35**, 2270–2282 (2019).
51. T. Otsubo, Y. Aso, K. Takimiya, Functional oligothiophenes as advanced molecular electronic materials. *J. Mater. Chem.* **12**, 2565–2575 (2002).
52. H. A. M. Ardoña, J. D. Tovar, Peptide π-Electron Conjugates: Organic Electronics for Biology? *Bioconjug. Chem.* **26**, 2290–2302 (2015).
53. K. Besar, H. A. M. Ardoña, J. D. Tovar, H. E. Katz, Demonstration of Hole Transport and Voltage Equilibration in Self-Assembled π-Conjugated Peptide Nanostructures Using Field-Effect Transistor Architectures. *ACS Nano*. **9**, 12401–12409 (2015).
54. E. R. Draper, J. J. Walsh, T. O. McDonald, M. A. Zwijnenburg, P. J. Cameron, A. J. Cowan, D. J. Adams, Air-stable photoconductive films formed from perylene bisimide gelators. *J. Mater.*

Chem. C. **2**, 5570–5575 (2014).

55. A. Meerschaut, L. Guemas, J. Rouxel, Structure and properties of the new phase of the pseudo one-dimensional compound TaS3. *J. Solid State Chem.* **36**, 118–123 (1981).
56. A. K. Rappé, C. J. Casewit, K. S. Colwell, W. A. Goddard, W. M. Skiff, UFF, a Full Periodic Table Force Field for Molecular Mechanics and Molecular Dynamics Simulations. *J. Am. Chem. Soc.* **114**, 10024–10035 (1992).
57. A. K. Rappé, W. A. Goddard, Charge equilibration for molecular dynamics simulations. *J. Phys. Chem.* **95**, 3358–3363 (1991).
58. G.-M. Mustata, Y. H. Kim, J. Zhang, W. F. DeGrado, G. Grigoryan, M. Wanunu, Graphene Symmetry Amplified by Designed Peptide Self-Assembly. *Biophys. J.* **110**, 2507–2516 (2016).
59. S. N. Kim, Z. Kuang, J. M. Slocik, S. E. Jones, Y. Cui, B. L. Farmer, M. C. McAlpine, R. R. Naik, Preferential Binding of Peptides to Graphene Edges and Planes. *J. Am. Chem. Soc.* **133**, 14480–14483 (2011).
60. T. F. A. De Greef, M. M. J. Smulders, M. Wolffs, A. P. H. J. Schenning, R. P. Sijbesma, E. W. Meijer, Supramolecular polymerization. *Chem. Rev.* **109**, 5687–5754 (2009).
61. M. Wehner, M. I. S. Röhr, M. Bühler, V. Stepanenko, W. Wagner, F. Würthner, Supramolecular Polymorphism in One-Dimensional Self-Assembly by Kinetic Pathway Control. *J. Am. Chem. Soc.* **141**, 6092–6107 (2019).
62. F. C. Spano, The Spectral Signatures of Frenkel Polarons in H- and J-Aggregates. *Acc. Chem. Res.* **43**, 429–439 (2010).
63. C. Adamo, D. Jacquemin, The calculations of excited-state properties with Time-Dependent Density Functional Theory. *Chem. Soc. Rev.* **42**, 845–856 (2013).
64. G. Macchi, B. M. Medina, M. Zambianchi, R. Tubino, J. Cornil, G. Barbarella, J. Gierschner, F. Meinardi, Spectroscopic signatures for planar equilibrium geometries in methyl-substituted oligothiophenes. *Phys. Chem. Chem. Phys.* **11**, 984–990 (2009).
65. F. Neese, The ORCA program system. *Wiley Interdiscip. Rev. Comput. Mol. Sci.* **2**, 73–78 (2012).
66. R. F. Fink, J. Seibt, V. Engel, M. Renz, M. Kaupp, S. Lochbrunner, H.-M. Zhao, J. Pfister, F. Würthner, B. Engels, Exciton Trapping in π-Conjugated Materials: A Quantum-Chemistry-Based Protocol Applied to Perylene Bisimide Dye Aggregates. *J. Am. Chem. Soc.* **130**, 12858–12859 (2008).
67. M. Abdel-Hafiez, R. Thiyagarajan, A. Majumdar, R. Ahuja, W. Luo, A. N. Vasiliev, A. A. Maarouf, S. G. Zybtsev, V. Y. Pokrovskii, S. V. Zaitsev-Zotov, V. V. Pavlovskiy, W. W. Pai, W. Yang, L. V. Kulik, Pressure-induced reentrant transition in NbS3 phases: Combined Raman

scattering and X-ray diffraction study. *Phys. Rev. B*. **99**, 235126 (2019).

68. Z. Wang, C. Sun, X. Xu, Y. Liu, Z. Chen, Y. “Michael” Yang, H. Zhu, Long-Range Hot Charge Transfer Exciton Dissociation in an Organic/2D Semiconductor Hybrid Excitonic Heterostructure. *J. Am. Chem. Soc.* **145**, 11227–11235 (2023).
69. Z. Liu, H. Qiu, C. Wang, Z. Chen, B. Zyska, A. Narita, A. Ciesielski, S. Hecht, L. Chi, K. Müllen, P. Samorì, Photomodulation of Charge Transport in All-Semiconducting 2D–1D van der Waals Heterostructures with Suppressed Persistent Photoconductivity Effect. *Adv. Mater.* **32**, 2001268 (2020).
70. R. Wahalathantrige Don, P. Das, Z. Ma, U. M. Kuruppu, D. Feng, B. Shook, M. K. Gangishetty, M. C. Stefan, N. R. Pradhan, C. N. Scott, Vinyl-Flanked Diketopyrrolopyrrole Polymer/MoS_2 Hybrid for Donor–Acceptor Semiconductor Photodetection. *Chem. Mater.* **35**, 4691–4704 (2023).
71. J. O. Island, A. J. Molina-Mendoza, M. Barawi, R. Biele, E. Flores, J. M. Clamagirand, J. R. Ares, C. Sánchez, H. S. J. van der Zant, R. D’Agosta, I. J. Ferrer, A. Castellanos-Gomez, Electronics and optoelectronics of quasi-1D layered transition metal trichalcogenides. *2D Mater.* **4**, 022003 (2017).
72. W. Wu, Y. Wang, Y. Niu, P. Wang, M. Chen, J. Sun, N. Wang, D. Wu, Z. Zhao, Thermal Localization Enhanced Fast Photothermoelectric Response in a Quasi-One-Dimensional Flexible NbS_3 Photodetector. *ACS Appl. Mater. Interfaces*. **12**, 14165–14173 (2020).
73. S.-L. Li, K. Tsukagoshi, E. Orgiu, P. Samorì, Charge transport and mobility engineering in two-dimensional transition metal chalcogenide semiconductors. *Chem. Soc. Rev.* **45**, 118–151 (2016).